Magnetic proximity effect of a topological insulator and a ferromagnet in thin-film bilayers of $Bi_{0.5}Sb_{1.5}Te_3$ and $SrRuO_3$

Gad Koren*

Physics Department, Technion—Israel Institute of Technology, Haifa 32000, Israel

(Received 13 November 2017; published 5 February 2018)

Magnetic proximity effect of a topological insulator in contact with a ferromagnet is reported in thin-film bilayers of 15-nm-thick $Bi_{0.5}Sb_{1.5}Te_3$ on either 15- or 40-nm-thick $SrRuO_3$ on (100) $SrTiO_3$ wafers. $SrRuO_3$ is an itinerant ferromagnet which has long been considered weak, thus any observation of a significant magnetic proximity effect in the present system should help elucidate the mechanism of this magnetism and might be utilized in device applications. Magnetotransport results of the bilayers were compared with those of reference films of 15-nm $Bi_{0.5}Sb_{1.5}Te_3$ and 15- or 40-nm $SrRuO_3$. Comparison of the temperature coefficient of resistance [$(1/R) \times dR/dT$, which is qualitatively proportional to the magnetization] of the bilayer and reference ferromagnetic film normalized above T_c shows a clear suppression in the bilayer by about 50% just below T_c, indicating a weaker proximity magnetization in the bilayer. Resistance hysteresis loops versus field at 1.85 ± 0.05 K in the bilayer and reference films show a clear magnetic proximity effect, where the peak resistance of the bilayer at the coercive field shifts to lower fields by $\sim$30% compared to a hypothetical bilayer of two resistors connected in parallel with no interaction between the layers. Narrowing of the coercive peaks of the bilayers as compared to those of the reference ferromagnetic films by 25–35% was also observed, which represents another signature of the magnetic proximity effect.

DOI: 10.1103/PhysRevB.97.054405

I. INTRODUCTION

Interactions between topological insulators (TIs) and magnetic materials, either ferromagnets (FMs) or antiferromagnets, are interesting due to the basic physics questions they raise as well as their possible potential application in spintronics and quantum computing [1–11]. These interactions, which basically originate in magnetic proximity effect (MPE), can induce long-range ferromagnetism in magnetically doped TIs at room temperature [4,12]. They can lead to spin or magnetization sensitive switching phenomena [5,13,14], to quantum anomalous Hall effect (quantum Hall effect without external magnetic field) [6,8,11,15–19], to weak-localization-like magnetoresistance effects [9], and so on. Some of the data are hard to reconcile with conventional MPE, such as the observation of Wei *et al.* [8] showing that in their TI-FM bilayer with a 1-nm-thick FM layer the magnetic moment was found to be larger by 60% than that of the FM magnetic ions. A conventional proximity effect can never induce stronger ferromagnetism in TI-FM bilayers just as it cannot induce stronger superconductivity in TI-S bilayers (where S is a superconductor) [20]. Therefore, it seems that unconventional MPE can be involved in TI-FM interfaces. MPE was observed even in S-FM heterostructures where evidence for induced magnetization in the superconductor was found by scanning electron spectroscopy [21]. Another issue is the sign of the induced magnetoresistance which can be positive or negative depending on the system involved [8,9,22].

In the present paper, TI-FM bilayers of the topological insulator $Bi_{0.5}Sb_{1.5}Te_3$ (BST) and the supposedly weak itinerant ferromagnet $SrRuO_3$ (SRO) with a ferromagnetic transition temperature $T_c = 150$ K are investigated, and a surprisingly strong conventional MPE with positive magnetoresistance is found.

II. PREPARATION AND BASIC PROPERTIES OF FILMS AND BILAYERS

SRO thin films on (100) $SrTiO_3$ (STO) were chosen for this paper as the ferromagnetic layers since these films are very well characterized in the literature [23,24]. $(Bi_xSb_{1-x})_2Te_3$ thin films were chosen as the topological insulator layers for the ability to tune their Fermi energy E_F to the Dirac point by changing the Bi doping x [25]. Both were prepared by laser ablation deposition in different vacuum chambers using the third harmonic of a Nd-YAG laser. Deposition was made on (100) STO wafers of 10×10 mm^2 area. The SRO films were deposited using a stoichiometric ceramic target of SRO under 70–90 mTorr of O_2 gas flow at 965 °C heater block temperature (about 800 °C on the surface of the wafer). The BST layers were deposited using a $Bi_{0.2}Sb_{1.8}Te_3$ target under vacuum and at 320 °C heater block temperature (about 250 °C on the surface of the wafer). Electron dispersive spectroscopy (EDS) measurements [26] showed that the resulting films were about 2.5 times richer in Bi than the target used yielding $Bi_{0.5}Sb_{1.5}Te_3$. Thus laser deposition is not as good as molecular-beam epitaxy for controlling the Bi and Sb content in these films [25]. The laser was operated at a pulse rate of 3.33 Hz, with fluence of $\sim$1.5 J/cm^2 on the target for the deposition of the SRO films, and lower fluence of $\sim$0.6 J/cm^2 for the deposition of

*gkoren@physics.technion.ac.il; http://physics.technion.ac.il/~gkoren

the BST layers. X-ray-diffraction measurements of our typical 15-nm-thick SRO reference film, and 15-nm-thick BST on a 15-nm-thick SRO bilayer (BL), showed that the SRO film grew epitaxially on the (100) STO wafer, while the BST cap layer grew in the hexagonal phase with preferential c-axis orientation normal to the wafer with $c = 3.04$ nm [26]. This yields five unit cells in a 15-nm-thick BST layer, leading to strong interactions between the top and bottom surface currents and basically resulting in a two-dimensional film. Atomic force microscopy images of the surface morphology of the 30-nm-thick bilayer showed good crystallization and ~3-4-nm rms roughness [26].

Bilayers with thicker SRO layers were also prepared and characterized. These were composed of 15-nm-thick BST film on a 40-nm-thick SRO layer on (100) STO wafers. Here we also added patterning of the SRO films and BST-SRO bilayers into a 30-cm-long meander line with 18-μm linewidth and 2-μm line spacing. Patterning was done under 13-mA/cm^2 Ar-ion milling at $-180\,^\circ$C to minimize damage to the samples. This allowed us to increase the measurement sensitivity by having a better signal-to-noise ratio, but at the cost of having a more dominant SRO signal and less sensitivity to the TI layer properties. Nevertheless, the basic MPE property in the BL of having narrower magnetoresistance peaks at the coercive fields as compared to those of the reference SRO film could already be seen also in this case. The transport measurements were done by the use of an array of 40 gold coated spring loaded spherical tips for the four-probe dc measurements on ten different locations on the wafer. All measurements on the unpatterned 15-nm BST on the 15-nm SRO bilayer and the 15-nm SRO reference film were made without additional contact pads (to keep surface cleanliness in between the deposition steps), while measurements on the meander lines were carried out using silver paste contact pads.

III. RESULTS AND DISCUSSION

A. 15-nm BST on 15-nm SRO bilayers and 15-nm SRO reference films

Figure 1 shows the resistance versus temperature results of a 30-nm-thick bilayer of 15-nm BST on 15-nm SRO together with the results on the 15-nm SRO reference film normalized to that of the bilayer at room temperature. One can easily see the bending down of both curves at the ferromagnetic transition at 150 K. These R versus T curves under zero-field cooling (ZFC) are quite close above T_c but become farther apart on cooling down below it. To demonstrate this more clearly, we plot here also the normalized ratio of the two curves R(BL ZFC)/[0.22 × R(SRO ZFC)], which clearly shows an almost constant behavior versus T above T_c and increasing values toward lower temperatures just below it. This is a clear signature of a MPE resulting from a suppressed rate of resistance decrease with decreasing temperature of the BL compared with that of the SRO film. Furthermore, should there be no interaction between the layers in the bilayer, adding the BST resistor in parallel to the SRO one should decrease the BL resistance and not increase it as is actually observed using the normalized SRO data in Fig. 1. Thus the existence of MPE in the BL follows. Also shown in this figure is the $R(T)$ under 1-T field cooling (FC) of the bilayer. The ZFC

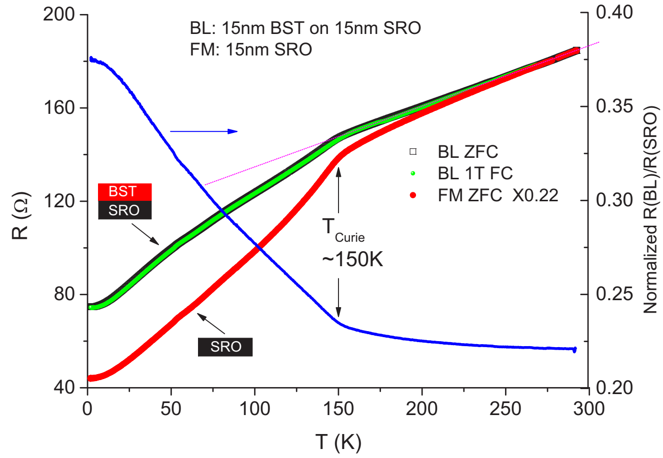

FIG. 1. Normalized resistance vs temperature of a 15-nm-thick SRO film under zero-field cooling, together with the corresponding results of the bilayer obtained by the deposition of a 15-nm-thick BST layer on it. Also shown are the R vs T curve of the bilayer under 1-T field cooling and the normalized ratio R(BL ZFC)/[0.22 × R(SRO ZFC)] vs T.

and the FC curves are quite indistinguishable with a very small magnetoresistance, which does not show any systematic behavior versus T, probably due to noise in the measurements.

Figure 2 presents the temperature coefficients of resistance (TCR) in percents per K $[100 \times (1/R) \times dR/dT]$ versus temperature under zero field of the 15-nm BST on the 15-nm SRO bilayer and of the 15-nm SRO reference film. These coefficients are useful indicators for the magnetic properties of the bilayer and film since they are qualitatively similar to the magnetization of the samples, as can be seen by the magnetic moment of a 200-nm-thick SRO film on (100) STO versus T, which is also plotted in this figure. This moment was measured by a superconducting quantum interference device magnetometer, and the reason for using such a thick film here is that the signal from the thinner 15-nm SRO was too noisy. The excess noise in the TCR curve of the 15-nm SRO film as

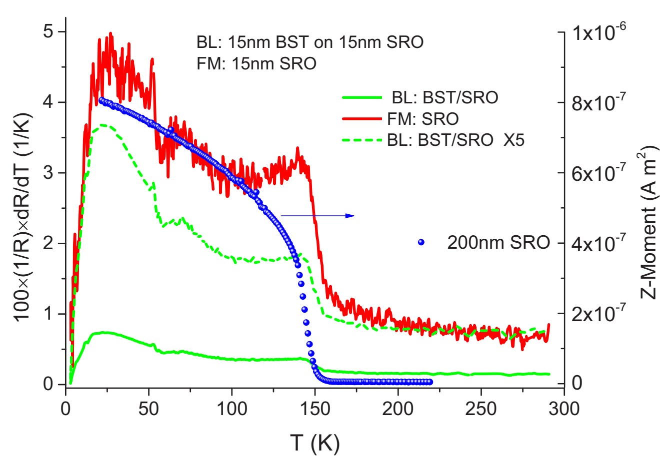

FIG. 2. Temperature coefficients of resistance (TCR) in percents per K $[100 \times (1/R) \times dR/dT]$ are plotted vs T for the 15-nm BST on the 15-nm SRO bilayer and the reference 15-nm SRO film. Also shown is the Z moment of a 200-nm-thick SRO film as measured by a superconducting quantum interference device magnetometer.

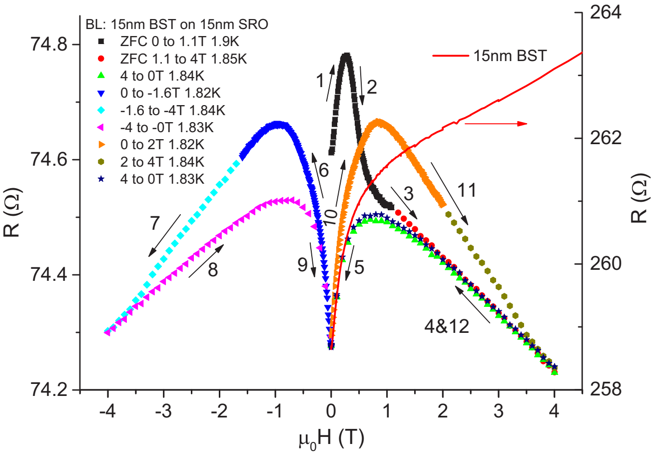

FIG. 3. Resistance hysteresis loops vs field normal to the wafer at 1.85 ± 0.05 K of the 15-nm BST on the 15-nm SRO bilayer, together with the nonhysteretic magnetoresistance of a 15-nm-thick BST film (red curve). The black arrows and numbers follow the magnetic history of the measurements.

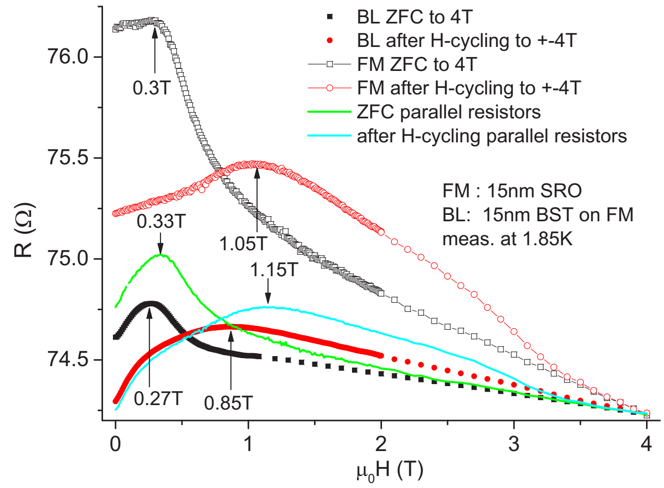

FIG. 4. Resistance vs field of the 15-nm BST on the 15-nm SRO bilayer under ZFC and after field cycling to ± 4 T, together with the corresponding R vs H of the reference 15-nm-thick SRO film normalized to the bilayer data at 4 T. Also shown is the resistance vs field of a hypothetical bilayer of 15-nm BST on 15-nm SRO calculated for two independent resistors connected in parallel with no interaction between the layers. The normalization factors for the SRO and the parallel resistors BST/SRO bilayer are 0.382 and 0.664, respectively.

compared to that of the bilayer is due to the noisy contacts on this very thin film as no contact pads were used in this measurement. This preserved a clean surface of this film which was then used for the deposition of the cap 15-nm BST layer on it to produce the bilayer. One can see that the sharp rise of the TCR and Z moment at $T_c = 150$ K is basically common to all curves. Also, above this temperature the curves are almost constants with a small fluctuation regime above T_c. Below 140 K, these curves, although rising with decreasing temperature down to about 20 K, are not proportional to one another and there is additional information in the TCR curves the origin of which is unclear at the present time. Below 20 K, the resistance of the BL and SRO film becomes quite constant (see Fig. 1), thus the TCR obviously goes to zero while the magnetization does not. We normalized the TCR curve of the bilayer to that of the SRO reference film in the paramagnetic regime above T_c in the range of 200–290 K in order to allow comparison between the two. We see that the TCR of the bilayer is suppressed by about 50% as compared to that of the reference film and this is a clear indication for the presence of a magnetic proximity effect in the bilayer. As no enhancement of the TCR in the bilayer is found as in [8], we conclude that the present results support the notion of a conventional MPE here.

Next we turn to resistance hysteresis loops measurements of the BL, TI, and SRO samples versus magnetic field at low temperature of 1.85 ± 0.05 K. Figure 3 depicts such measurement results of the 15-nm BST on the 15-nm SRO bilayer, together with the nonhysteretic R versus H curve of a second reference film of the TI (15-nm-thick BST on a (100) STO wafer) [27]. By increasing the field after ZFC from 0 to 4 T, the resistance shows a peak at 0.26 T which results from the combined effect of the weak antilocalization (WAL) in the 15-nm BST layer where the magnetoresistance increases with field [27], and the resistance decrease due to realignment of the magnetic domains in the SRO layer of the bilayer. The latter originates in reduction of the overall domain-wall resistance [24] due to merging of domains with increasing field into a single domain. We also note here that part of the decrease of the magnetoresistance with increasing field is due to a parabolic background which was clearly observed in our samples also above T_c at about 175 K. With decreasing field down to 0 T, R retraces the former curve down to about 1.5 T, and then bends down following the WAL curve of the reference BST film. Further decrease of the field down to -4 T reveals quite a broad peak in the range of -0.5 to -1.5 T with a maximum at -0.85 T, which can be identified as the coercive field of the bilayer. By sweeping the field up to $+4$ T and back to zero field, a symmetric result is obtained.

To check for a signature of MPE in the bilayer, we present in Fig. 4 the positive field data of Fig. 3, together with the R versus H data of the 15-nm-thick SRO reference film. All data were normalized at 4 T, which is much above the coercive fields of both the BL and SRO samples. One can see that the magnetoresistance after ZFC of the SRO film has only a small increase with field up to a peak at 0.3 T beyond which it goes down with increasing field similar to data in the literature with the measuring bias current parallel to the magnetic domain walls [24]. This peak is located at a higher field than that of the bilayer (0.3 versus 0.27 T). A similar shift of the corresponding peak after field cycling (the coercive field peak) is also observed (1.05 T for the SRO film versus 0.85 T for the bilayer). To demonstrate that these shifts are due to MPE in the bilayer, we plotted in Fig. 4 also the expected magnetoresistance of a hypothetical bilayer with no interaction between the layers using a simple addition of parallel resistors of the resistances of the stand-alone SRO and BST films. This yields magnetoresistance peaks at 0.33 T after ZFC and 1.15 T after field cycling. Thus comparison with the magnetoresistance peaks of the real bilayer at 0.27 and 0.85 T, respectively, shows a clear suppression of these coercive fields as expected from MPE in a bilayer where magnetic interactions between the layers are present.

B. Meander lines of 15-nm BST on 40-nm SRO bilayers and 40-nm SRO reference films

Now we turn to magnetoresistance of bilayers with a thicker SRO base layer. Here the magnetic properties are more robust and similar to those of the bulk SRO, and those of the TI have a much smaller effect on the magnetoresistance results near zero field due to their WAL property. As explained before, we also patterned these bilayers and reference SRO film into long meander lines in order to increase the sensitivity of the measurements. Figure 5 shows the magnetoresistance data of a meander line patterned in one step on a 15-nm-thick BST on a 40-nm-thick SRO bilayer. As one can see the data are quite similar to results on thick SRO films where the measuring bias current is perpendicular to the orientation of the domain walls (no upturn near zero field after ZFC) [24]. Again, to check for MPE we compared these data with those of the reference 40-nm-thick SRO film (see inset). One can see that the coercive field peak shift of the SRO reference film to higher fields compared to that of the BL is now quite small, but the width of the former is about 30% higher than that of the latter (0.29 versus 0.22 T). This is a clear signature of MPE, though we know of no theory that explains this behavior. Possibly, magnetic fluctuations are suppressed more in the bilayer than in the stand-alone SRO film due to pinning of the domain walls at the TI-FM interface.

Figure 6 depicts magnetoresistance data of a 15-nm BST on a 40-nm SRO bilayer again, but unlike in Fig. 5 the sample was prepared using two separated patterning steps with measurements after each step. First, the base layer of a 40-nm SRO film was deposited and patterned into a 30-cm-long meander line, and its magnetoresistance hysteresis loops were measured. Then the cap layer of 15-nm BST was deposited on it

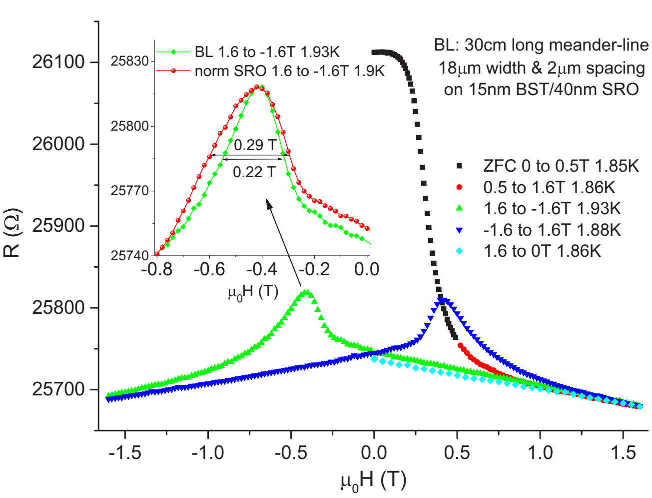

FIG. 5. Resistance hysteresis loops vs magnetic field normal to the wafer at 1.89 ± 0.04 K of a 30-cm-long meander line of 18-μm width and 2-μm spacing patterned on a 15-nm BST on a 40-nm SRO bilayer. Inset: The left-hand side peak together with the data of the corresponding 40-nm SRO reference meander line normalized to the maximum peak resistance of the bilayer.

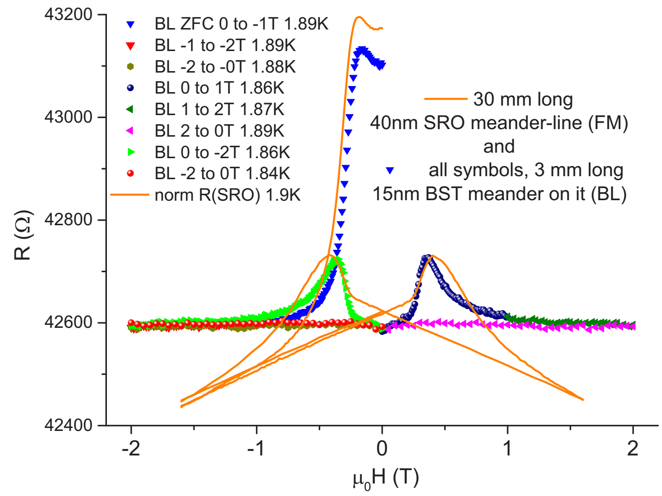

FIG. 6. Resistance hysteresis loops vs magnetic field normal to the wafer at 1.87 ± 0.03 K of two meander lines of 18-μm width and 2-μm spacing. One is 30 cm long and patterned on a 40-nm-thick SRO layer, and the other is of 15-nm BST deposited on it and repatterned (the bilayer meander line). Only a 3-cm-long segment of the latter was measured here. The data of the SRO reference meander line were normalized to those of the peak maxima at the coercive field of the TI-FM bilayer (at ± 0.35 T).

and repatterned with the same meander-line mask overlapping the first one in the base layer. The magnetoresistance measurements were repeated on the final bilayer, and the data of both measurements at 1.9 K are depicted in Fig. 6. The results of the SRO base meander were normalized to those of the final bilayer at the maxima of coercive field peaks. The shifts and widths of the coercive peaks of the bilayer as compared to those of the SRO meander line are similar to those of Fig. 5, but both are more pronounced here. The bilayer shifts are larger and the widths are narrower, possibly due to a more resistive interface in Fig. 6. This could originate in residues left over after the patterning process of the base SRO layer, that later affected the results of the bilayer. The flat bilayer background signal in Fig. 6 as compared to Fig. 5 might be a result of this effect.

The overall picture that emerges from the results of Figs. 3–6 is that the magnetoresistance signal after ZFC is large, its shape versus field can be affected by the TI layer (Figs. 3 and 4), and it apparently masks the smaller peaks at the coercive field H_{coer} which occur at higher fields. We shall thus discuss only the coercive peaks after field cycling. For the bilayers with 15-nm-thick SRO we find $H_{coer} = 0.85$ T and for the stand-alone SRO layer $H_{coer} = 1.05$ T, while for the bilayers with 40-nm-thick SRO the corresponding results are 0.41–0.36 and 0.42–0.41 T, respectively. Clearly, the H_{coer} of thinner SRO layers are higher than those of the thicker ones, which indicates weaker magnetic interactions and smaller domain size in the thinner films [28]. This affects the H_{coer} values of the bilayers in a similar way. The shifts and widths of the coercive peaks of the bilayers compared to the reference ferromagnetic films are more interesting. All the magnetoresistance results of the bilayers show shifts of H_{coer} to lower fields and narrowing of the corresponding peaks as compared to the results of the SRO films indicating a clear

MPE. Comparing the H_{coer} values of the peak positions in Fig. 4 we find 1.15 T for the noninteracting BL (two resistors in parallel), which is larger than the measured 1.05 T in the SRO reference layer, which is larger still than the 0.85 T of the BL. All these are clear indications that there are strong magnetic interactions between the layers of the bilayer, and demonstrate a strong magnetic proximity effect in the present TI-FM bilayers.

IV. CONCLUSIONS

By comparing measurement results of resistance versus temperature and magnetoresistance at low temperatures of TI-FM bilayers to those of a reference SRO film, signatures of magnetic proximity effect in the bilayers were found. These included suppression of the TCR in the bilayers, as well as shifts of the coercive fields to lower fields, and narrowing of the corresponding coercive peaks in the bilayers as compared to the reference SRO films. The supposedly weak itinerant ferromagnetism of SRO seems to induce a surprisingly robust MPE in BST-SRO bilayers.

ACKNOWLEDGMENTS

We are grateful to Yoichi Ando for useful discussions, and to Yaron Jarach for the EDS measurements of the BST film stoichiometry.

[1] M. Z. Hassan and C. L. Kane, Colloquium: Topological insulators, Rev. Mod. Phys. **82**, 3045 (2010).

[2] J. E. Moore, The birth of topological insulators, Nature (London) **464**, 194 (2010).

[3] A. Yu. Kitaev, Fault-tolerant quantum computation by anyons, Ann. Phys. **303**, 2 (2003).

[4] I. Vobornik, U. Manju, J. Fujii, F. Borgatti, P. Torelli, D. Krizmancic, Y. S. Hor, R. J. Cava, and G. Panaccione, Magnetic proximity effect as a pathway to spintronic applications of topological insulators, Nano Lett. **11**, 4079 (2011).

[5] F. Yang, S. Ghatak, A. A. Taskin, K. Segawa, Y. Ando, M. Shiraishi, Y. Kanai, K. Matsumoto, A. Rosch, and Y. Ando, Switching of charge-current-induced spin polarization in the topological insulator $BiSbTeSe_2$, Phys. Rev. B **94**, 075304 (2016).

[6] M. Li, C.-Z. Chang, B. J. Kirby, M. E. Jamer, W. Cui, L. Wu, P. Wei, Y. Zhu, D. Heiman, Ju Li, and J. S. Moodera, Proximity-Driven Enhanced Magnetic Order at Ferromagnetic-Insulator–Magnetic-Topological-Insulator Interface, Phys. Rev. Lett. **115**, 087201 (2015).

[7] M. Li, W. Cui, J. Yu, Z. Dai, Z. Wang, F. Katmis, W. Guo, and J. Moodera, Magnetic proximity effect and interlayer exchange coupling of ferromagnetic/topological insulator/ferromagnetic trilayer, Phys. Rev. B **91**, 014427 (2015).

[8] P. Wei, F. Katmis, B. A. Assaf, H. Steinberg, P. Jarillo-Herrero, D. Heiman, and J. S. Moodera, Exchange-Coupling-Induced Symmetry Breaking in Topological Insulators, Phys. Rev. Lett. **110**, 186807 (2013).

[9] Qi I. Yang, M. Dolev, Li Zhang, J. Zhao, A. D. Fried, E. Schemm, M. Liu, A. Palevski, A. F. Marshall, S. H. Risbud, and A. Kapitulnik, Emerging weak localization effects on a topological insulator–insulating ferromagnet (Bi_2Se_3-EuS) interface, Phys. Rev. B **88**, 081407(R) (2013).

[10] T. Hesjedal and Y. Chen, Engineered heterostructures, Nat. Mater. **16**, 3 (2017).

[11] H. Weng, R. Yu, X. Hu, Xi Dai, and Z. Fang, Quantum anomalous Hall effect and related topological electronic states, Adv. Phys. **64**, 227 (2015).

[12] F. Katmis, V. Lauter, F. S. Nogueira, B. A. Assaf, M. E. Jamer, P. Wei, B. Satpati, J. W. Freeland, I. Eremin, D. Heiman, P. Jarillo-Herrero, and J. S. Moodera, A high-temperature ferromagnetic topological insulating phase by proximity coupling, Nature (London) **533**, 513 (2016).

[13] Q. L. He, X. Kou, A. J. Grutter, G. Yin, L. Pan, X. Che, Y. Liu, T. Nie, B. Zhang, S. M. Disseler, B. J. Kirby, W. Ratcliff II, Q. Shao, K. Murata, X. Zhu, G. Yu, Y. Fan, M. Montazeri, X. Han, J. A. Borchers, and K. L. Wang, Tailoring exchange couplings in magnetic topological-insulator/antiferromagnet heterostructures, Nat. Mat. **16**, 94 (2017).

[14] Y. Fan, X. Kou, P. Upadhyaya, Q. Shao, L. Pan, M. Lang, X. Che, J. Tang, M. Montazeri, K. Murata, Li-Te Chang, M. Akyol, G. Yu, T. Nie, K. L. Wong, J. Liu, Y. Wang, Y. Tserkovnyak, and K. L. Wang, Electric-field control of spin-orbit torque in a magnetically doped topological insulator, Nature Nanotech. **11**, 352 (2016).

[15] Zilong Jiang, Cui-Zu Chang, C. Tang, J.-G. Zheng, J. S. Moodera, and J. Shi, Structural and proximity-induced ferromagnetic properties of topological insulator–magnetic insulator heterostructures, AIP Adv. **6**, 055809 (2016).

[16] C.-X. Liu, S.-C. Zhang, and X.-L. Qi, The quantum anomalous Hall effect: Theory and experiment, Annu. Rev. Condens. Matter Phys. **7**, 301 (2016).

[17] C.-Z. Chang, W. Zhao, D. Y. Kim, P. Wei, J. K. Jain, C. Liu, M. H. W. Chan, and J. S. Moodera, Zero-Field Dissipationless Chiral Edge Transport and the Nature of Dissipation in the Quantum Anomalous Hall State, Phys. Rev. Lett. **115**, 057206 (2015).

[18] A. Kandala, A. Richardella, S. Kempinger, C.-X. Liu, and N. Samarth, Giant anisotropic magnetoresistance in a quantum anomalous Hall insulator, Nat. Commun. **6**, 7434 (2015).

[19] X. Kou, L. Pan, J. Wang, Y. Fan, E. S. Choi, Wei-Li Lee, T. Nie, K. Murata, Q. Shao, S.-C. Zhang, and K. L. Wang, Metal-to-insulator switching in quantum anomalous Hall states, Nat. Commun. **6**, 8474 (2015).

[20] G. Koren, Proximity effects at the interface of a superconductor and a topological insulator in NbN-Bi_2Se_3 thin film bilayers, Supercond. Sci. Technol. **28**, 025003 (2015).

[21] I. Asulin, O. Yuli, G. Koren, and O. Millo, Evidence for induced magnetization in superconductor-ferromagnet heterostructures: A scanning tunneling spectroscopy study, Phys. Rev. B **79**, 174524 (2009).

[22] J. S. Moodera, L. R. Kinder, T. M. Wong, and R. Meservey, Large Magnetoresistance at Room Temperature in Ferromagnetic Thin Film Tunnel Junctions, Phys. Rev. Lett. **74**, 3273 (1995).

[23] A. F. Marshall, L. Klein, J. S. Dodge, C. H. Ahn, J. W. Reiner, L. Mieville, L. Antagonazza, A. Kapitulnik, T. H. Geballe, and M. R. Beasley, Lorentz transmission electron microscope

study of ferromagnetic domain walls in $SrRuO_3$: Statics, dynamics, and crystal structure correlation, J. Appl. Phys. **85**, 4131 (1999).

[24] L. Klein, Y. Kats, A. F. Marshall, J. W. Reiner, T. H. Geballe, M. R. Beasley, and A. Kapitulnik, Domain Wall Resistivity in $SrRuO_3$, Phys. Rev. Lett. **84**, 6090 (2000).

[25] J. Zhang, Cui-Zu Chang, Z. Zhang, J. Wen, X. Feng, K. Li, M. Liu, Ke He, L. Wang, Xi Chen, Qi-Kun Xue, X. Ma, and Y. Wang, Band structure engineering in $(Bi_{1-x}Sb_x)_2Te_3$ ternary topological insulators, Nat. Commun. **2**, 574 (2011).

[26] See Supplemental Material at http://link.aps.org/supplemental/10.1103/PhysRevB.97.054405 for structural, morphological, transport, and stoichiometry properties of the presently used $(Bi_xSb_{1-x})_2Te_3$ laser ablated films and their bilayers with $SrRuO_3$.

[27] G. Koren, Magnetoresistance, gating and proximity effects in ultrathin NbN-Bi_2Se_3 bilayers, Condens. Matter **2**, 14 (2017).

[28] L. Klein, J. S. Dodge, T. H. Geballe, A. Kapitulnik, A. F. Marshall, L. Antognazza, and K. Char, Perpendicular magnetic anisotropy and strong magneto-optic properties of $SrRuO_3$ epitaxial films, Appl. Phys. Lett. **66**, 2427 (1995).